Topological superconductivity of line defects in transition metal dichalcogenides

Xiaoming Zhang ●,[1,*] Huidong Wang,[1] Jiale Liu,[1] Mingwen Zhao,[2,†] and Feng Liu[3]

[1]*College of Physics and Optoelectronic Engineering, Ocean University of China, Qingdao, Shandong 266100, China*
[2]*School of Physics, Shandong University, Jinan, Shandong 250100, China*
[3]*Department of Materials Science and Engineering, University of Utah, Salt Lake City, Utah 84112, USA*

Convincing signatures of Majorana zero modes (MZMs) are one necessary requirement for achieving fault-tolerant quantum computations based on topological superconductivity (TSC). In addition to improving fabrication techniques, exploring the stoichiometric TSC platform is another route to suppressing the influences of trivial in-gap modes on the signatures of MZMs. Stoichiometric transition metal dichalcogenides (TMD) with topological surface states (TSSs) are promising but the field range of inducing magnetic vortices to harbor MZMs is limited by the small perpendicular upper critical field. Here, we propose that the line defects of chalcogen vacancies (CVs) embedded in TMDs are the stoichiometric TSC candidates for realizing stable MZMs without needing the TSSs under a wide range of in-plane magnetic fields. Detailed analysis and calculations on the 1H-MoX_2, 1H-WX_2, and 1T-PtX_2 ($X = S$, Se, or Te) monolayers with CV line defects indicate the antisymmetric spin-orbit coupling effect, known as the origin of odd-parity pairing, is ensured by noncentrosymmetric point group symmetry. First-principles TSC phase diagrams are constructed to facilitate experimental detection of convincing signatures for the MZMs located at both ends of the line defect. Our findings enrich the stoichiometric TSC candidates and will promote device fabrication to manipulating and storing quantum information based on the device-friendly TMDs.

I. INTRODUCTION

The Majorana zero mode (MZM) of topological super-conductivity (TSC) is one appearing form of non-Abelian anyon with exactly zero energy and its localized wave function is split into two spatially separated halves, which enables topological-protected manipulation and nonlocal storage of quantum information [1,2]. Given the rarity of intrinsic *p*-wave superconductors with TSC [3], the effective TSC theory of manifesting an effective odd-parity pairing gap from *s*-wave ones was developed by employing topological surface states (TSSs) or the antisymmetric spin-orbit coupling (SOC) effect [4–7]. This stimulates extensive research attention to capture the signatures of MZM through making hybrid devices of nanowire with strong SOC [8–10], constructing heterostructures of superconductors and topological insulators (TIs) [11], tuning atom compositions in iron-based super-conductors [12–14], and so on. During this process, one predicament is the presence of trivial in-gap modes, which may lead the evidence for the emergence of nontrivial MZMs being less convincing.

The trivial in-gap modes could be induced by smooth chemical potentials, partial proximity effect of superconductors, random disorders and impurities, etc. These inhomogeneities are especially significant when the TSC candidates need sophisticated heterostructure fabrication or sensitive

composition tuning. In addition to improving fabrication techniques [15], another feasible route to observing convincing signatures of MZMs is exploring the homogeneous materials of the stoichiometric composition. Recently, stoichiometric iron pnictides with TSSs were investigated and the existence of MZMs has been verified in CaKFe$_4$As$_4$ [16] and LiFeAs [17], and the LiFeAs can be strained to form an ordered and tunable MZM lattice [18]. Moreover, anisotropic MZM in magnetic vortices [19], spin-orbit-parity coupled super-conductivity [20], and the nodeless superconducting gap of TSSs [21,22] reveal the stoichiometric transition metal dichalcogenides (TMDs) 2M-WS$_2$ as a promising TSC candidate. Furthermore, the spectroscopic evidence of MZM at magnetic vortices was found in the natural compound of 4Hb-TaS$_2$ that interleaves superconducting 1H-TaS$_2$ layers with strongly correlated 1T-TaS$_2$ layers [23]. The research on stoichiometric TSC candidates represents a step forward toward realizing topological quantum computation.

Given the well-developed TMD-related techniques, a series of theoretical works predict the gap functions of stoichiometric 1H-TMDs possibly exhibiting mixed-parity pairing states [24–35], stemming from the Ising SOC effect induced spin-valley locking. When the odd-parity component is dominant, these TSC candidates favor forming stable Majo-rana edge modes, while the field range of inducing magnetic vortices to harbor MZMs will be limited by the small perpen-dicular upper critical field of Ising superconductivity [36,37]. One can glimpse the limitation from the perpendicular field of 0.36 T for 2M-WS$_2$ [19] and of 0.1–0.2 T for 4Hb-TaS$_2$ [23] when observing the signatures of MZM, which is far smaller

————————
*zxm@ouc.edu.cn
†zmw@sdu.edu.cn

than that ($\sim$2 T) of CaKFe$_4$As$_4$ [16] and that (0.5–6 T) of LiFeAs [17,18]. Evoking MZM by employing an in-plane magnetic field represents a promising direction to expand the field range [30], because the in-plane upper critical field of two-dimensional (2D) TMDs can reach up to several times the Pauli paramagnetic limit due to the Ising pairing and the absence of the orbital pair-breaking effect [36,37].

In this paper, we propose the one-dimensional (1D) chalcogen vacancy (CV) line defects embedded in stoichiometric TMD semiconductors can realize stable MZMs under an in-plane magnetic field. This proposal is supported by the fact that the structural imperfections are inevitable and the CVs are the most abundant native defects [38–40], which can be generated and engineered during and after the synthesis of TMDs [41–46]. The agglomeration of CVs will enable 1D line defects with the orientation being favorable in the zigzag (ZZ) direction [47–51] and being sensitive to mechanical strain [49–51]. We show the MZMs exponentially localize at both ends of the line defect and could be experimentally detected by referring to our constructed TSC phase diagrams. The 1D TSC phases established on 2D layered TMD materials will promote the device fabrication used for manipulating and storing quantum information.

II. RESULTS

A. Electronic property of CV line defect in TMDs

A TMD monolayer crystallizes in a hexagonal structure with the stoichiometry of MX_2, where the metal atoms M (groups IV–VIII) locate at the middle plane and covalently bond with two chalcogen atom X ($X = S$, Se, or Te) planes at both sides [52,53]. Depending on the species of M and X atoms, TMD monolayers can be semiconductors or metals. Considering a semiconducting gap providing the energy range of accommodating defect states free from the interference of bulk states, we focus on the TMD semiconductors with the sandwiched metal atoms M being Mo, W, or Pt. Structurally, MoX_2 and WX_2 are usually stable at the 1H noncentrosymmetric phase with the three atomic planes stacking in an ABA order [Figs. 1(a)–1(c)], while PtX_2 tends to form the 1T centrosymmetric phase with an ABC stacking order [Figs. 1(d)–1(f)]. The line defects in these TMD semiconductors are constructed by the nearest neighbor (NN) CVs along the ZZ direction [Figs. 1(a) and 1(d)], by the next NN (N^3) CVs along the ZZ direction [Figs. 1(b) and 1(e)], and by the NN CVs along the armchair (AC) direction [Figs. 1(c) and 1(f)], which are abbreviated as ZZCV, N^{3}ZZCV, and ACCV line defect, respectively.

To compare the relative feasibility of these line defects in experimental synthesis, we calculated their formation energy E_{form} (Table I) by using first-principles calculations, as detailed in the Supplemental Material (SM) [54] that includes Refs. [36,37,55–82]. Under the same preparing conditions, the E_{form} of ZZCVs is smaller than that of ACCVs and N^{3}ZZCVs for 1H-MX_2. This indicates the ZZCVs are easily formed in 1H-MX_2, consistent with the experimental report that the CVs usually agglomerate along the ZZ direction [47–50]. The E_{form}'s of N^{3}ZZCVs and ACCVs in the same MX_2 are comparable with each other. For the 1T-PtX_2, we find the ZZCVs
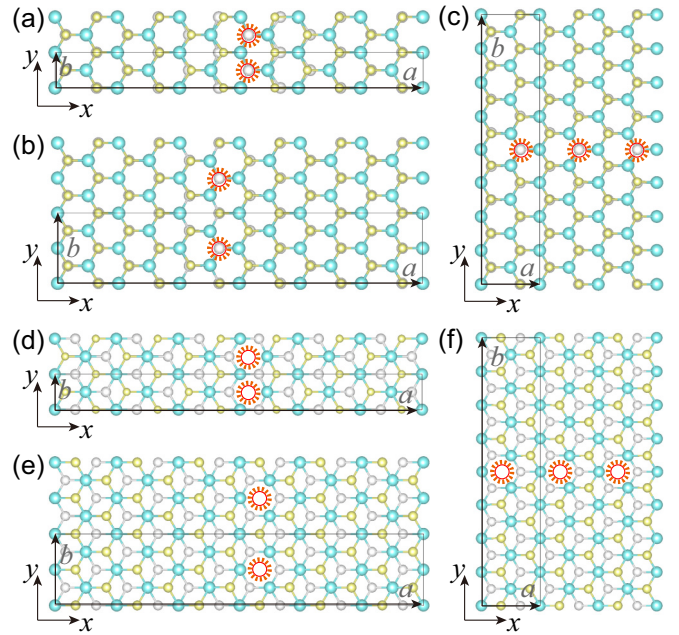

FIG. 1. The schematic of (a), (d) ZZCV, (b), (e) N^{3}ZZCV, and (c), (f) ACCV line defects in (a)–(c) 1H- and (d)–(f) 1T-TMD monolayer. The black rectangle represents the periodic cell of TMD semiconductors with the embedded CV (red dashed circles) line defects.

tend to form in 1T-PtS$_2$, while ACCVs and N^{3}ZZCVs are more favorable in 1T-PtTe$_2$. There is no dominant orientation for the CV line defects in 1T-PtSe$_2$ because of the nearly equal E_{form}, which is supported by the experimental observation that the pairing of Se point vacancies could form along both the ZZ and AC directions in PtSe$_2$ [51]. Notably, our calculations have not considered the effect of lattice shrinkage and stretching, which provide efficient knobs to altering the E_{form} and hence engineering the types of CV line defects [49–51]. Consequently, all three types of CV line defect are concentrated to exploring the feasibility of evoking the TSC phase from the associated defect states. We suggest preparing the CV line defect in the MX_2 semiconductors under M-rich

TABLE I. The E_{form} under M-rich and X-rich conditions for the three types of CV line defect in the considered TMD semiconductor. E_{form} is shown in units of eV.

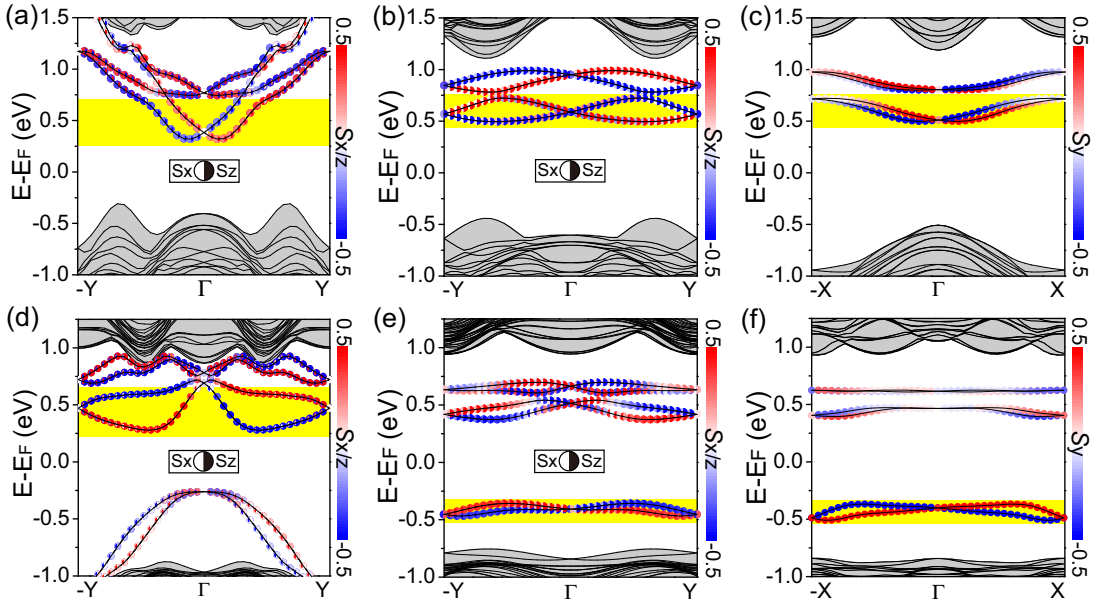|	M-rich ZZCV	M-rich N^{3}ZZCV	M-rich ACCV	X-rich ZZCV	X-rich N^{3}ZZCV	X-rich ACCV
MoS$_2$	0.82	1.05	1.05	2.16	2.40	2.40
MoSe$_2$	1.03	1.34	1.33	2.26	2.57	2.56
MoTe$_2$	1.04	1.70	1.73	1.63	2.30	2.32
WS$_2$	1.10	1.30	1.29	2.32	2.52	2.51
WSe$_2$	1.23	1.54	1.54	2.26	2.57	2.57
WTe$_2$	1.27	1.89	1.88	1.56	2.18	2.16
PtS$_2$	1.07	1.16	1.13	1.42	1.51	1.48
PtSe$_2$	1.27	1.28	1.25	1.85	1.85	1.83
PtTe$_2$	1.19	0.96	0.98	1.68	1.46	1.48

FIG. 2. The band structures of (a)–(c) 1H-WS$_2$ and (d)–(f) 1T-PtS$_2$ monolayer with (a), (d) ZZCV, (b), (e) N^{3}ZZCV, and (c), (f) ACCV line defects. The nonzero spin expectation values S_x and S_z are represented by the colors filled in the left and right half of the circles on the defect states of the ZZ directed line defects, respectively. The nonzero S_y is represented by the colors fully filled in the circles on the defect states of AC directed line defects.

conditions because of the lower formation energy than that under X-rich conditions (Table I).

The electronic band structures of the considered 1H- and 1T-TMD monolayers with CV line defects are calculated by using first-principles calculations (as detailed in the SM [54]). The line defects of 1H-WS$_2$ lead to two defect states in its energy gap [Figs. 2(a)–2(c)]. Due to the absence of local inversion symmetry, the spin degeneracy of each defect state is lifted by the antisymmetric SOC effect, which is featured by spin-orbit splitting and spin-momentum locking. The spin-momentum locking can be shown more clearly by calculating the expectation value of the spin component for a given k point with the eigenstate $\varphi(k)$ via $S_i(k) = \langle\varphi(k)|\sigma_i|\varphi(k)\rangle$. Here σ_i ($i = x, y, z$) is a Pauli matrix in spin space. We can see the S_x and S_z are both nonzero for the ZZCV [Fig. 2(a)] and N^{3}ZZCV [Fig. 2(b)] line defect, while the nonzero spin component is S_y for the ACCV line defect [Fig. 2(c)]. The complete plots of S_i are also presented in Fig. S1 [54]. For the line defects in 1T-PtS$_2$, three defect states with significant spin-orbit splitting and spin-momentum locking are induced in its energy gap [Figs. 2(d)–2(f)]. The spin-momentum locking is identical to that of 1H-WS$_2$, i.e., nonzero S_x and S_z for the line defect along the ZZ direction [Figs. 2(d) and 2(e)] and nonzero S_y for the ACCV one [Fig. 2(f)], which can also be seen from Fig. S2 [54]. The spin-orbit splitting and spin-momentum locking are consistent with previous reports [60,61,83–87].

To reveal the physical origin of the spin-momentum locking observed on the defect states, we analyze their effective SOC Hamiltonians based on the **k·p** perturbation theory combined with group theory. The point group of the considered CV line defects in 1H-WS$_2$ and 1T-PtS$_2$ are all noncentrosymmetric C_s, which contains the identity operation E and

a mirror operation M_y: $y \rightarrow -y$. From the character table of C_s, the components of wave vector $\boldsymbol{k}$ and Pauli matrix $\boldsymbol{\sigma}$ are sorted out for the irreducible representation A' and A'', i.e., A': k_x, k_z, σ_y; A'': k_y, σ_x, σ_z. According to the direct product table of C_s, one can be aware that the SOC includes the terms of $k_x\sigma_y$, $k_y\sigma_x$, and $k_y\sigma_z$ near the Γ point, but the term of $k_z\sigma_y$ is forbidden because k_z is not a good quantum number in the 2D TMD monolayers within the xy plane. With this analysis in mind, we construct an antisymmetric SOC Hamiltonian including NN interactions in the whole Brillouin zone:

$$h_{\text{SOC}}(k) = 2\lambda^x_{\text{ZZ}}\sin(bk_y)\sigma_x + 2\lambda^y_{\text{AC}}\sin(ak_x)\sigma_y$$
$$- 2\lambda^z_{\text{ZZ}}\sin(bk_y)\sigma_z. \tag{1}$$

Here a (b) represents the length of lattice vector $\boldsymbol{a(b)}$ along the x (y) direction (see Fig. 1), and $k_{x/y}$ is the x/y component of momentum. λ^x_{ZZ} and λ^y_{AC} are, respectively, the NN interspin interaction along the ZZ and AC directions, while λ^z_{ZZ} represents the NN intraspin interaction along the ZZ directions. Nonzero λ^x_{ZZ}, λ^y_{AC}, and λ^z_{ZZ} will lead to nonzero spin expectation values of S_x, S_y, and S_z locked with the k_y, k_x, and k_y, respectively.

The specific values for the parameters of λ^x_{ZZ}, λ^y_{AC}, and λ^z_{ZZ} can be extracted from a first-principles Hamiltonian obtained by fitting each defect state under the basis of the Wannier function (WF), as detailed in the SM [54]. Considering the similar spin-momentum locking, we fit the defect states with large spin-orbit splitting in the energy gap of 1H-WS$_2$ and 1T-PtS$_2$ (highlighted by yellow in Fig. 2), and related analysis is applicable to other in-gap defect states. The extracted values are summarized in Fig. 3. One can clearly see that λ^x_{ZZ} and λ^z_{ZZ} are nonzero for the ZZCV [Fig. 3(a)] and N^{3}ZZCV [Fig. 3(b)]
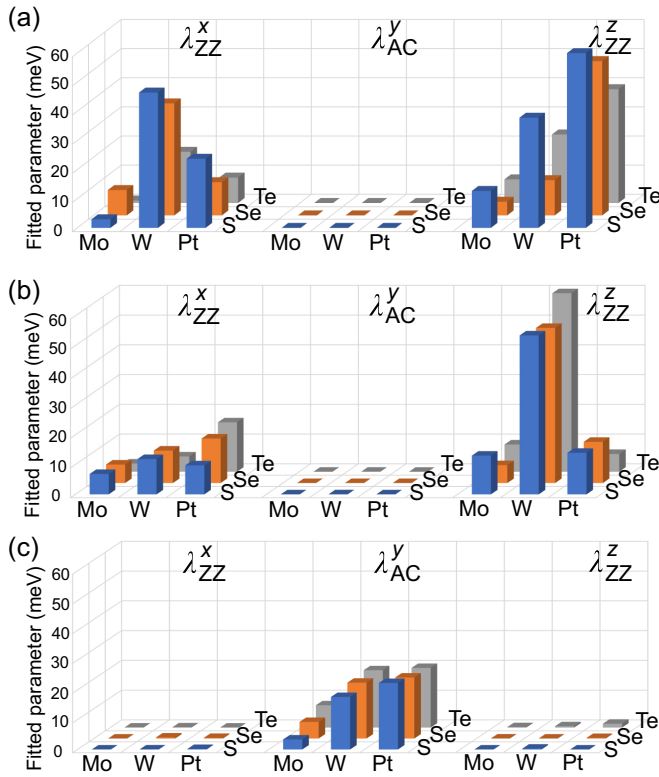
FIG. 3. Analyzing the parameters in the effective SOC Hamiltonian. The fitted values of λ_{ZZ}^x, λ_{AC}^y, and λ_{ZZ}^z for the defect states of CV line defects along the (a) ZZCV, (b) N^{3}ZZCV, and (c) ACCV line defects in our considered TMD semiconductors.

line defect in both 1H-WS$_2$ and 1T-PtS$_2$, indicating the S_x and S_z are locked with the k_y. Accordingly, the nonzero parameter of λ_{AC}^y in Fig. 3(c) locks S_y and k_x together for the ACCV line defect. The spin-momentum locking features are consistent with our first-principles calculations on the spin expectation values of in-gap defect states (Fig. 2).

This point group symmetry ensured spin-momentum locking is further confirmed by extensive first-principles calculations on other 2D TMD semiconductors with CV line defects, including 1H-WSe$_2$ (Fig. S3), 1H-WTe$_2$ (Fig. S4), 1T-PtSe$_2$ (Fig. S5), 1T-PtTe$_2$ (Fig. S6), 1H-MoS$_2$ (Fig. S7), 1H-MoSe$_2$ (Fig. S8), and 1H-MoTe$_2$ (Fig. S9) [54]. Our calculations reveal the spin-momentum locking on the defect states in these TMD semiconductors is similar to that of 1H-WS$_2$ and 1T-PtS$_2$. The similarity can be alternatively captured by fitting the in-gap defect states in Figs. S3–S9 [54], because the magnitudes of extracted values for the parameters in Eq. (1) present the same distributions among all the TMD monolayers, i.e., nonzero λ_{ZZ}^x and λ_{ZZ}^z for ZZ directed line defects [Figs. 3(a) and 3(b)], and nonzero λ_{AC}^y for AC directed ones [Fig. 3(c)]. The physical origin of the similarity is attributed to the fact that all the considered TMD monolayers with CV line defects share the identical noncentrosymmetric point group of C_s. We emphasize that the analysis of the antisymmetric SOC effect is applicable to the CV line defects in TMD semiconductors with lattice shrinkage and stretching [49–51], as long as the C_s point group symmetry is well preserved.

B. TSC of CV line defect in TMDs

We will take the 1H-WS$_2$ and 1T-PtS$_2$ with CV line defect as representative examples to illustrate the feasibility of sparking 1D TSC phases from the in-gap defect states. This can be done by constructing a first-principles Bogoliubov–de Gennes (BdG) Hamiltonian [63–66]:

$$H_{WF}^{BdG}(\boldsymbol{k})$$
$$= \begin{pmatrix} h_{WF}(\boldsymbol{k}) + h(M) - E_0 & i\Delta\sigma_y \\ -i\Delta\sigma_y^* & -h_{WF}^*(-\boldsymbol{k}) - h(M) + E_0 \end{pmatrix}.$$
$$(2)$$

In this expression, E_0 is the energy of defect states that condense s-wave pairing Δ. $h(M) = M(\nu\sigma_x + \mu\sigma_y)$ represents the in-plane magnetic field, whose orientation is controlled by the coefficients of ν and μ with the constraint $\nu^2 + \mu^2 = 1$. The field magnitude M can exceed the Pauli paramagnetic limit in Ising superconductors [36,37]. $h_{WF}(\boldsymbol{k})$ denotes the above mentioned first-principles Hamiltonian under the basis of WF, which can exactly reproduce the electronic band structures of in-gap defect states obtained directly from first-principles calculations.

Diagonalizing $H_{WF}^{BdG}(\boldsymbol{k})$ will enable us to determine the TSC phase transition for the defect states with a given energy by analyzing the dependence of the pairing gap on the in-plane magnetic field. At time reversal invariant momenta (TRIM) with Kramers degeneracy (KD), we find the direct pairing gap (DPG) closes when the magnitudes of the magnetic field and s-wave pairing satisfy the relation of $M = \sqrt{\Delta^2 + (E_0 - E_{KD})^2}$, regardless of the directions of magnetic field and line defects [see black lines in Figs. 4(a)–4(f) and Figs. S10–S15 [54]]. Here E_{KD} is the energy where the is KD locating. The closed DPG can be reopened when $M > \sqrt{\Delta^2 + (E_0 - E_{KD})^2}$ for most cases, which indicates the emergence of TSC phase transition. The only exception is the AC directed line defect under the magnetic field along the y direction, where the DPG cannot be reopened (see the black region in Figs. S12(f) and S15(f) [54]). This is attributed to the electron spins of defect states being fully polarized to the y direction [Fig. 3(c)].

The TSC phase transitions induced by the DPG reopening are confirmed by analyzing the 1D version of the Berry phase, i.e., the Zak phase [88]. The Zak phase γ_n of the nth BdG band is defined as the integral of Berry connection, $\gamma_n = i \int_{-\pi}^{\pi} \langle u_{nk} | \partial_k | u_{nk} \rangle dk$. Here $|u_{nk}\rangle$ is the periodic part of the BdG Bloch wave function. The total Zak phase γ of DPG is obtained by summing the γ_n of the BdG bands below the pairing gap. The calculated γ's for the represented parameters marked by the red dots (γ_R) and green squares (γ_G) in the TSC phase diagrams [Figs. 4(a)–4(f)] are shown in Fig. 4(g). Because the Zak phase is a gauge-dependent quantity, the total Zak phase is not always quantized to 0 or π. Despite this, the difference between the Zak phases $\delta\gamma = |\gamma_R - \gamma_G|$ is uniquely defined, which can be regarded as topological invariant and employed to distinguishing topological classes [89]. One can clearly see that $\delta\gamma$ is exactly equal to π for all the considered CV line defects [Fig. 4(g)], indicating the DPG reopening indeed induces TSC phase transition.
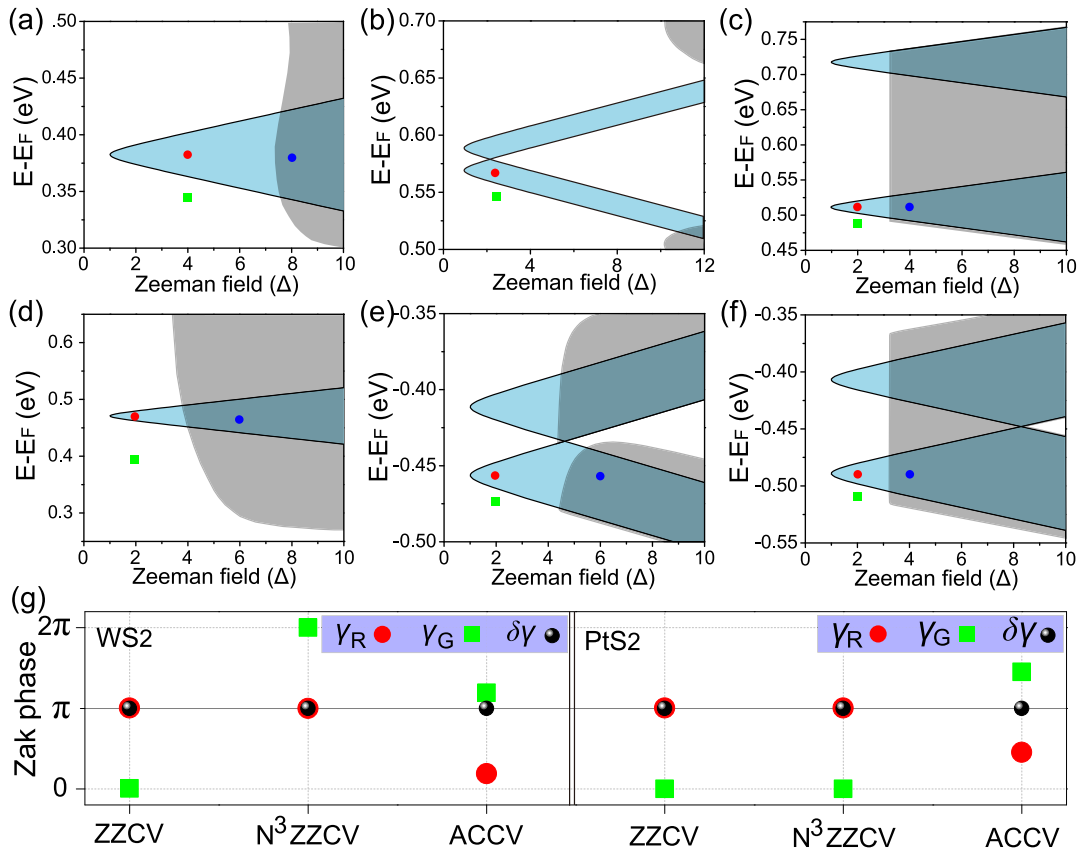
FIG. 4. (a)–(f) The TSC phase diagrams of (a), (d) ZZCV, (b), (e) N^3ZZCV, and (c), (f) ACCV line defects in (a)–(c) 1H-WS$_2$ and (d)–(f) 1T-PtS$_2$. The angle between the direction of magnetic field (with the unit of Δ) and line defect was set to 0.1π. The parameter spaces of the TSC phase are highlighted in light blue, and the gray regions represent the spaces with negative GPG. (g) The Zak phase γ_R and γ_G calculated by using the parameters marked by red and green dots in (a)–(f). $\delta\gamma$ is the difference between the γ_R and γ_G.

Next, we further analyze the variation of the global pairing gap (GPG) under an in-plane magnetic field. The GPG is defined as the minimum value among the direct and indirect pairing gaps in the whole Brillouin zone, which will be set to zero when the direct one is closed. Different from the DPG at TRIM, the magnitude of GPG shows high dependence on the directions of the magnetic field and line defect. If the magnetic fields are not parallel to the direction of the line defect, the GPG will change from positive to zero and then to negative values with the increase of the magnetic field. The parameter spaces with negative GPG are marked by gray in Figs. 4(a)–4(f) and in Figs. S10–S15 [54], which clearly indicates the gray colored spaces increase with the increase of angles between the directions of the magnetic field and line defect. This trend is attributed to the interaction between the field and the nonzero in-plane spin component (Fig. 3). Despite this, the DPGs are not closed at those k points except TRIM during this process, which indicates the critical point of TSC phase translation remains unchanged. The negative GPG will be absent when the field is applied to the direction of the line defect (see Figs. S10(a), S11(a), S12(a), S13(a), S14(a), and S15(a) [54]).

We emphasize that the GPG is critical for the stability of MZMs endowed by the 1D TSC phase, which can be illustrated by calculating the energy spectrum of superconducting quasiparticles. For the 1H-WS$_2$ with the ZZCV line

defect, the fully opened positive GPG can be seen from the spectrum [Fig. 5(a)] by using the parameters marked by the red dot in the parameter space of the TSC phase [Fig. 4(a)]. The corresponding MZMs can be revealed by calculating the probability density of the BdG quasiparticle eigenstates with different energy in real space [Fig. 5(b)]. One can clearly see the zero energy MZMs exponentially and stably localize at both ends of the line defect, while the eigenstates with nonzero energy are not spatially localized. The stable MZMs are expected to be always maintained by using the proximity effect of superconductivity if the GPG is positive. For the parameters marked by the blue dot in Fig. 4(a), the GPG is negative but the DPG at each k point is always positive [Fig. 5(c)], which we term as the "continuously" opened gap. Despite the nontriviality of this parameter space, the absence of positive GPG lead to the hybridization between the MZM and trivial bulk quasiparticle states, which destroys the stability of the MZM [Fig. 5(d)]. The hybridization with bulk states or trivial in-gap modes may be one reason for the experimentally measured zero-bias peak deviating from the quantized conductance plateau of $2e^2/h$ [8–10]. The field orientation dependent MZM was also experimentally reported in nanowire topological superconductors [90,91]. Similar results can be reached for the N^3ZZCV line defect in 1H-WS$_2$ (Fig. S16), ACCV in 1H-WS$_2$ (Fig. S17), ZZCV in 1T-PtS$_2$ (Fig. S18), N^3ZZCV in 1T-PtS$_2$ (Fig. S19), and ACCV in
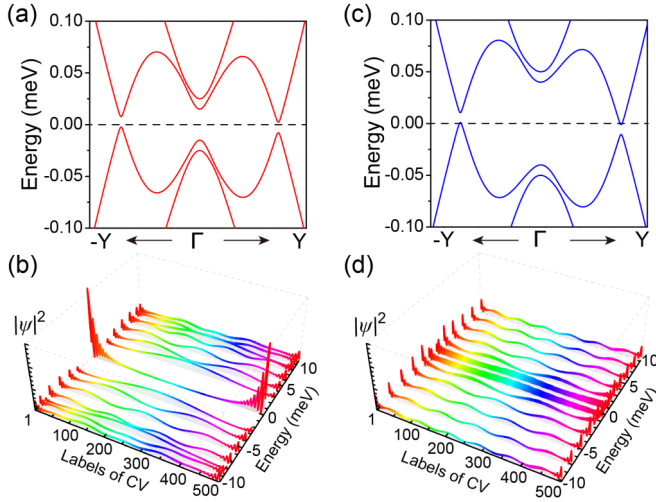
FIG. 5. (a), (c) The BdG quasiparticle spectrum and (b), (d) the real-space distributions of the BdG eigenstates with different energies in the ZZCV line defect of 1H-WS$_2$. The (a), (b) positive and (c), (d) negative GPGs are simulated by using the parameters marked by red and blue dots in Fig. 4(a), respectively. The length of the line defect is 500 CVs, where the end boundaries are labeled by 1 and 500.

1T-PtS$_2$ (Fig. S20) [54], which are simulated by using the parameters marked by the red and blue dots in Figs. 4(b), S11(c), and 4(d)–4(f), respectively. The TSC phase diagrams will provide guidance for experimentally detecting convincing signatures of MZMs locating at both ends of the line defect.

III. DISCUSSION

We demonstrate the CV line defects in stoichiometric TMD semiconductors to be promising 1D TSC candidates. This proposal not only avoids making hybrid devices, constructing heterostructures, and tuning atom compositions, but also eliminates the need of TSSs and/or unconventional superconductivity in defect-free TMD materials. In addition to natural generation under fluctuating growth conditions using chemical vapor deposition, the CV line defects can be more deliberately achieved in TMD materials by ion/electron irradiation, plasma treatments, and high-temperature annealing [41–43]. This well-developed technique will enable one to construct desired structural patterns of MZMs for manipulating and storing quantum information.

We suggest preparing the experimental platforms with the predicted 1D TSC phase of unoccupied in-gap defect states by growing the defective TMD monolayer on bulk TMD and then covering a defect-free TMD monolayer. The superconductivity of conductive bands in the outermost layer can be achieved by using gating, which is robust against the in-plane magnetic field [36,37]. The doping concentration is highest in the outermost defect-free TMD monolayer, and the relatively lower concentration of the inner defect TMD monolayer is expected to partially fill the in-gap defect states with antisymmetric SOC. Then the superconductivity of defect states is expected to be induced by the superconducting proximity effect of the outermost layer [92]. For the occupied in-gap defect states,

one promising route to introducing desired superconductivity is interleaving superconducting TMD layers [23]. In addition to the gating method, it was reported that charge doping can be achieved by a modulation doping strategy [67–72]. We have found this strategy is also applicable to dope the TMD semiconductors with CV line defects by encapsulating a BN monolayer, as elaborated in the SM [54].

The 1D TSC phase of CV line defects is highly dependent on specific parameters, which need to be finely tuned during experimental confirmation. To realize convincing signatures of MZM, the negative GPG should be excluded by regulating the energy of defect states that condense s-wave pairing and/or by tuning the magnitudes/directions of the in-plane field. The regulation rule in turn can be considered as the evidence of existing MZMs. The parameter space with a stable MZM is largest when the field direction is parallel to the direction of the line defect, which will make the stable MZM easier to detect. One can maintain the exotic MZMs up to the in-plane upper critical field of Ising superconductors, where the field range is several times the Pauli paramagnetic limit. This fact is one advantage of the CV line defects along the ZZ and AC directions, where the C_s point group symmetry forbids the spin polarizing to the direction of the line defect. To further reveal the advantages, we consider a CV line defect violating the C_s point group symmetry in 1H-WS$_2$ (Fig. S24(a) [54]) and 1T-PtS$_2$ (Fig. S24(b) [54]), which could also realize the desired TSC phase with a stable MZM under a proper in-plane magnetic field. However, the spin expectation values S_x, S_y, and S_z are all nonzero for their corresponding in-gap defect states (Figs. S25(a) and S26(a) [54]), which hinders the formation of the TSC phase diagram without negative GPG (Figs. S25(b)–S25(g) and Figs. S26(b)–S26(g) [54]).

We emphasize that the defect states that could enable the 1D TSC phase are not limited to the CVs but can be extended to other type of defects in stoichiometric TMD semiconductors. The candidates include the experimentally achieved defects of metal vacancies [93] and substitutional dopants [94–96], which possess in-gap defect states similar to those of CVs. The 1D metallic states, localized at the inversion domains, grain boundaries, and dislocations in TMD [43,44], serve as other promising platforms to realize a stable MZM. The stoichiometric TMDs provide a frame to constrain the embedded line defects experiencing homogeneous chemical potentials and the superconducting proximity effect, which are beneficial for eliminating the trivial in-gap modes and thus achieving convincing signatures of MZMs. Notably, different from the embedded quantum structures in a monolayer Fe(Te,Se) superconductor [97,98] that demands sensitive composition tuning and unconventional superconductivity, our proposal is employing the widely existing conventional superconductivity, which can, in principle, be extended to the defect states in the abundant conventional superconductors with stoichiometric composition.

IV. CONCLUSION

The CV line defects in 2D stoichiometric TMDs 1H-WX_2, 1H-MoX_2, and 1T-PtX_2 ($X = S$, Se or Te) are proposed to be promising platforms for realizing the 1D TSC phase. The desired antisymmetric SOC is ensured by

noncentrosymmetric point group symmetry, and the needed in-plane magnetic field is less destructive to the superconductivity. TSC phase transitions are determined by reopening the DPG at TRIM, which indeed can be achieved by the defect states of CV line defects under an in-plane magnetic field. We reveal the MZMs are only stable for the TSC phase with positive GPG, but will hybridize with the trivial bulk BdG quasiparticle states for a negative one. TSC phase diagrams indicate one can avoid the negative GPG and achieve convincing signatures of the MZM by tuning the field magnitudes/directions, regulating the energy of defect states that condense s-wave pairing, and engineering the orientation of line defects. Our findings are of significant importance for enriching the stoichiometric TSC candidates where the MZMs survive under a wide range

of magnetic field, facilitating the detection of convincing MZM signatures and the application of fault-tolerant quantum computations based on the well-developed techniques of TMDs.

[1] A. Y. Kitaev, Fault-tolerant quantum computation by anyons, Ann. Phys. **303**, 2 (2003).

[2] C. Nayak, S. H. Simon, A. Stern, M. Freedman, and S. Das Sarma, Non-Abelian anyons and topological quantum computation, Rev. Mod. Phys. **80**, 1083 (2008).

[3] A. Y. Kitaev, Unpaired Majorana fermions in quantum wires, Phys.-Usp **44**, 131 (2001).

[4] L. Fu and C. L. Kane, Superconducting proximity effect and Majorana fermions at the surface of a topological insulator, Phys. Rev. Lett. **100**, 096407 (2008).

[5] R. M. Lutchyn, J. D. Sau, and S. Das Sarma, Majorana fermions and a topological phase transition in semiconductor-superconductor heterostructures, Phys. Rev. Lett. **105**, 077001 (2010).

[6] Y. Oreg, G. Refael, and F. von Oppen, Helical liquids and majorana bound states in quantum wires, Phys. Rev. Lett. **105**, 177002 (2010).

[7] X. Zhang, J. Liu, and F. Liu, Topological superconductivity based on antisymmetric spin–orbit coupling, Nano Lett. **22**, 9000 (2022).

[8] S. M. Frolov, M. J. Manfra, and J. D. Sau, Topological superconductivity in hybrid devices, Nat. Phys. **16**, 718 (2020).

[9] E. Prada, P. San-Jose, M. W. A. de Moor, A. Geresdi, E. J. H. Lee, J. Klinovaja, D. Loss, J. Nygård, R. Aguado, and L. P. Kouwenhoven, From Andreev to Majorana bound states in hybrid superconductor–semiconductor nanowires, Nat. Rev. Phys. **2**, 575 (2020).

[10] K. Flensberg, F. von Oppen, and A. Stern, Engineered platforms for topological superconductivity and Majorana zero modes, Nat. Rev. Mater. **6**, 944 (2021).

[11] Z. Zhu, H. Zheng, and J.-F. Jia, Majorana zero mode in the vortex of artificial topological superconductor, J. Appl. Phys. **129**, 151104 (2021).

[12] L.-Y. Kong and H. Ding, Emergent vortex Majorana zero mode in iron-based superconductors, Acta Phys. Sin. **69**, 110301 (2020).

[13] G. Li, S. Zhu, D. Wang, Y. Wang, and H.-J. Gao, Recent progress of scanning tunneling microscopy/spectroscopy study of Majorana bound states in the FeTe$_{0.55}$Se$_{0.45}$ superconductor, Supercond. Sci. Technol. **34**, 073001 (2021).

[14] X. Wang, C. Chen, T. Zhang, T. Zhang, and D. Feng, STM study on the vortex states and Majorana zero-modes in FeSe-based high-T_c superconductors, Quantum Front. **1**, 12 (2022).

[15] P. Marra, Majorana nanowires for topological quantum computation, J. Appl. Phys. **132**, 231101 (2022).

[16] W. Liu, L. Cao, S. Zhu, L. Kong, G. Wang, M. Papaj, P. Zhang, Y.-B. Liu, H. Chen, G. Li, F. Yang, T. Kondo, S. Du, G.-H. Cao, S. Shin, L. Fu, Z. Yin, H.-J. Gao, and H. Ding, A new Majorana platform in an Fe-As bilayer superconductor, Nat. Commun. **11**, 5688 (2020).

[17] L. Kong, L. Cao, S. Zhu, M. Papaj, G. Dai, G. Li, P. Fan, W. Liu, F. Yang, X. Wang, S. Du, C. Jin, L. Fu, H.-J. Gao, and H. Ding, Majorana zero modes in impurity-assisted vortex of LiFeAs superconductor, Nat. Commun. **12**, 4146 (2021).

[18] M. Li, G. Li, L. Cao, X. Zhou, X. Wang, C. Jin, C.-K. Chiu, S. J. Pennycook, Z. Wang, and H.-J. Gao, Ordered and tunable Majorana-zero-mode lattice in naturally strained LiFeAs, Nature (London) **606**, 890 (2022).

[19] Y. Yuan, J. Pan, X. Wang, Y. Fang, C. Song, L. Wang, K. He, X. Ma, H. Zhang, F. Huang, W. Li, and Q.-K. Xue, Evidence of anisotropic Majorana bound states in 2M-WS$_2$, Nat. Phys. **15**, 1046 (2019).

[20] E. Zhang, Y.-M. Xie, Y. Fang, J. Zhang, X. Xu, Y.-C. Zou, P. Leng, X.-J. Gao, Y. Zhang, L. Ai, Y. Zhang, Z. Jia, S. Liu, J. Yan, W. Zhao, S. J. Haigh, X. Kou, J. Yang, F. Huang, K. T. Law, F. Xiu, and S. Dong, Spin–orbit–parity coupled superconductivity in atomically thin 2M-WS$_2$, Nat. Phys. **19**, 106 (2023).

[21] Y. W. Li, H. J. Zheng, Y. Q. Fang, D. Q. Zhang, Y. J. Chen, C. Chen, A. J. Liang, W. J. Shi, D. Pei, L. X. Xu, S. Liu, J. Pan, D. H. Lu, M. Hashimoto, A. Barinov, S. W. Jung, C. Cacho, M. X. Wang, Y. He, L. Fu *et al.*, Observation of topological superconductivity in a stoichiometric transition metal dichalcogenide 2M-WS$_2$, Nat. Commun. **12**, 2874 (2021).

[22] S. Cho, S. Huh, Y. Fang, C. Hua, H. Bai, Z. Jiang, Z. Liu, J. Liu, Z. Chen, Y. Fukushima, A. Harasawa, K. Kawaguchi, S. Shin, T. Kondo, Y. Lu, G. Mu, F. Huang, and D. Shen, Direct observation of the topological surface state in the topological superconductor 2M-WS$_2$, Nano Lett. **22**, 8827 (2022).

[23] A. K. Nayak, A. Steinbok, Y. Roet, J. Koo, G. Margalit, I. Feldman, A. Almoalem, A. Kanigel, G. A. Fiete, B. Yan, Y. Oreg, N. Avraham, and H. Beidenkopf, Evidence of topological boundary modes with topological nodal-point superconductivity, Nat. Phys. **17**, 1413 (2021).

[24] N. F. Q. Yuan, K. F. Mak, and K. T. Law, Possible topological superconducting phases of MoS_2, Phys. Rev. Lett. **113**, 097001 (2014).

[25] M. A. Rahimi, A. G. Moghaddam, C. Dykstra, M. Governale, and U. Zülicke, Unconventional superconductivity from magnetism in transition-metal dichalcogenides, Phys. Rev. B **95**, 104515 (2017).

[26] Y.-T. Hsu, A. Vaezi, M. H. Fischer, and E.-A. Kim, Topological superconductivity in monolayer transition metal dichalcogenides, Nat. Commun. **8**, 14985 (2017).

[27] E. Sosenko, J. Zhang, and V. Aji, Unconventional superconductivity and anomalous response in hole-doped transition metal dichalcogenides, Phys. Rev. B **95**, 144508 (2017).

[28] Y. Nakamura and Y. Yanase, Odd-parity superconductivity in bilayer transition metal dichalcogenides, Phys. Rev. B **96**, 054501 (2017).

[29] M. R. Aliabad and M.-H. Zare, Proximity-induced mixed odd- and even-frequency pairing in monolayer $NbSe_2$, Phys. Rev. B **97**, 224503 (2018).

[30] W.-Y. He, B. T. Zhou, J. J. He, N. F. Q. Yuan, T. Zhang, and K. T. Law, Magnetic field driven nodal topological superconductivity in monolayer transition metal dichalcogenides, Commun. Phys. **1**, 40 (2018).

[31] D. Möckli and M. Khodas, Robust parity-mixed superconductivity in disordered monolayer transition metal dichalcogenides, Phys. Rev. B **98**, 144518 (2018).

[32] D. Möckli and M. Khodas, Magnetic-field induced $s+if$ pairing in Ising superconductors, Phys. Rev. B **99**, 180505(R) (2019).

[33] W. Chen, Q. Zhu, Y. Zhou, and J. An, Topological Ising pairing states in monolayer and trilayer TaS_2, Phys. Rev. B **100**, 054503 (2019).

[34] C. Lane and J.-X. Zhu, Identifying topological superconductivity in two-dimensional transition-metal dichalcogenides, Phys. Rev. Mater. **6**, 094001 (2022).

[35] A. Julku, J. J. Kinnunen, A. Camacho-Guardian, and G. M. Bruun, Light-induced topological superconductivity in transition metal dichalcogenide monolayers, Phys. Rev. B **106**, 134510 (2022).

[36] W. Li, J. Huang, X. Li, S. Zhao, J. Lu, Z. V. Han, and H. Wang, Recent progresses in two-dimensional Ising superconductivity, Mater. Today Phys. **21**, 100504 (2021).

[37] J. Lu, O. Zheliuk, Q. Chen, I. Leermakers, N. E. Hussey, U. Zeitler, and J. Ye, Full superconducting dome of strong Ising protection in gated monolayer WS_2, Proc. Natl. Acad. Sci. USA **115**, 3551 (2018).

[38] H.-P. Komsa and A. V. Krasheninnikov, Native defects in bulk and monolayer MoS_2 from first principles, Phys. Rev. B **91**, 125304 (2015).

[39] H.-P. Komsa, J. Kotakoski, S. Kurasch, O. Lehtinen, U. Kaiser, and A. V. Krasheninnikov, Two-dimensional transition metal dichalcogenides under electron irradiation: Defect production and doping, Phys. Rev. Lett. **109**, 035503 (2012).

[40] J.-Y. Noh, H. Kim, and Y.-S. Kim, Stability and electronic structures of native defects in single-layer MoS_2, Phys. Rev. B **89**, 205417 (2014).

[41] S. Wang, A. Robertson, and J. H. Warner, Atomic structure of defects and dopants in 2D layered transition metal dichalcogenides, Chem. Soc. Rev. **47**, 6764 (2018).

[42] Q. Liang, Q. Zhang, X. Zhao, M. Liu, and A. T. S. Wee, Defect engineering of two-dimensional transition-metal dichalcogenides: Applications, challenges, and opportunities, ACS Nano **15**, 2165 (2021).

[43] Z. Lin, B. R. Carvalho, E. Kahn, R. Lv, R. Rao, H. Terrones, M. A. Pimenta, and M. Terrones, Defect engineering of two-dimensional transition metal dichalcogenides, 2D Mater. **3**, 022002 (2016).

[44] H.-P. Komsa and A. V. Krasheninnikov, Engineering the electronic properties of two-dimensional transition metal dichalcogenides by introducing mirror twin boundaries, Adv. Electron. Mater. **3**, 1600468 (2017).

[45] M. Zhou, W. Wang, J. Lu, and Z. Ni, How defects influence the photoluminescence of TMDCs, Nano Res. **14**, 29 (2021).

[46] H. Tian, C. Ren, and S. Wang, Valleytronics in two-dimensional materials with line defect, Nanotechnology **33**, 212001 (2022).

[47] S. Wang, G.-D. Lee, S. Lee, E. Yoon, and J. H. Warner, Detailed atomic reconstruction of extended line defects in monolayer MoS_2, ACS Nano **10**, 5419 (2016).

[48] Q. Chen, H. Li, S. Zhou, W. Xu, J. Chen, H. Sawada, C. S. Allen, A. I. Kirkland, J. C. Grossman, and J. H. Warner, Ultralong 1D vacancy channels for rapid atomic migration during 2D void formation in monolayer MoS_2, ACS Nano **12**, 7721 (2018).

[49] H.-P. Komsa, S. Kurasch, O. Lehtinen, U. Kaiser, and A. V. Krasheninnikov, From point to extended defects in two-dimensional MoS_2: Evolution of atomic structure under electron irradiation, Phys. Rev. B **88**, 035301 (2013).

[50] S. Fang, Y. Wen, C. S. Allen, C. Ophus, G. G. D. Han, A. I. Kirkland, E. Kaxiras, and J. H. Warner, Atomic electrostatic maps of 1D channels in 2D semiconductors using 4D scanning transmission electron microscopy, Nat. Commun. **10**, 1127 (2019).

[51] J. Chen, J. Zhou, W. Xu, Y. Wen, Y. Liu, and J. H. Warner, Atomic-level dynamics of point vacancies and the induced stretched defects in 2D monolayer $PtSe_2$, Nano Lett. **22**, 3289 (2022).

[52] S. Manzeli, D. Ovchinnikov, D. Pasquier, O. V. Yazyev, and A. Kis, 2D transition metal dichalcogenides, Nat. Rev. Mater. **2**, 17033 (2017).

[53] P. Wang, Y. Yang, E. Pan, F. Liu, P. M. Ajayan, J. Zhou, and Z. Liu, Emerging phases of layered metal chalcogenides, Small **18**, 2105215 (2022).

[54] See Supplemental Material at http://link.aps.org/supplemental/10.1103/PhysRevB.108.144101 for details of first-principles calculations, charge doping achieved by modulation doping strategy, and supplemental Figs. S1–S26, which includes Refs. [36,37,55–82].

[55] G. Kresse and J. Furthmüller, Efficiency of *ab-initio* total energy calculations for metals and semiconductors using a plane-wave basis set, Comput. Mater. Sci. **6**, 15 (1996).

[56] P. Hohenberg and W. Kohn, Inhomogeneous electron gas, Phys. Rev. **136**, B864 (1964).

[57] W. Kohn and L. J. Sham, Self-consistent equations including exchange and correlation effects, Phys. Rev. **140**, A1133 (1965).

[58] J. P. Perdew, K. Burke, and M. Ernzerhof, Generalized gradient approximation made simple, Phys. Rev. Lett. **77**, 3865 (1996).

[59] P. E. Blöchl, Projector augmented-wave method, Phys. Rev. B **50**, 17953 (1994).

[60] M. A. U. Absor, I. Santoso, Harsojo, K. Abraha, F. Ishii, and M. Saito, Defect-induced large spin-orbit splitting in monolayer PtSe$_2$, Phys. Rev. B **96**, 115128 (2017).

[61] M. A. U. Absor, I. Santoso, N. Yamaguchi, and F. Ishii, Spin splitting with persistent spin textures induced by the line defect in the 1T phase of monolayer transition metal dichalcogenides, Phys. Rev. B **101**, 155410 (2020).

[62] G. Pizzi, V. Vitale, R. Arita, S. Blügel, F. Freimuth, G. Géranton, M. Gibertini, D. Gresch, C. Johnson, T. Koretsune, J. Ibañez-Azpiroz, H. Lee, J.-M. Lihm, D. Marchand, A. Marrazzo, Y. Mokrousov, J. I. Mustafa, Y. Nohara, Y. Nomura, L. Paulatto *et al.*, WANNIER90 as a community code: New features and applications, J. Phys.: Condens. Matter. **32**, 165902 (2020).

[63] X. Zhang, K.-H. Jin, J. Mao, M. Zhao, Z. Liu, and F. Liu, Prediction of intrinsic topological superconductivity in Mn-doped GeTe monolayer from first-principles, npj Comput. Mater. **7**, 44 (2021).

[64] X. Zhang and F. Liu, Prediction of Majorana edge states from magnetized topological surface states, Phys. Rev. B **103**, 024405 (2021).

[65] X. Zhang, D. Gao, X. Zhu, J. Liu, W. Wang, X. Liu, and M. Zhao, Prediction of topological superconductivity from type-IV, -III, -II, and -I′ nodal points induced by Rashba spin-orbit coupling, Phys. Rev. B **104**, 245409 (2021).

[66] X. Zhang and F. Liu, Fulde-Ferrell-Larkin-Ovchinnikov pairing induced by a Weyl nodal line in an Ising superconductor with a high critical field, Phys. Rev. B **105**, 024505 (2022).

[67] D. Wang, X.-B. Li, and H.-B. Sun, Modulation doping: A strategy for 2D materials electronics, Nano Lett. **21**, 6298 (2021).

[68] Y. Cho, G. R. Schleder, D. T. Larson, E. Brutschea, K.-E. Byun, H. Park, P. Kim, and E. Kaxiras, Modulation doping of single-layer semiconductors for improved contact at metal interfaces, Nano Lett. **22**, 9700 (2022).

[69] Y. Wang, J. Balgley, E. Gerber, M. Gray, N. Kumar, X. Lu, J.-Q. Yan, A. Fereidouni, R. Basnet, S. J. Yun, D. Suri, H. Kitadai, T. Taniguchi, K. Watanabe, X. Ling, J. Moodera, Y. H. Lee, H. O. H. Churchill, J. Hu, L. Yang *et al.*, Modulation doping via a two-dimensional atomic crystalline acceptor, Nano Lett. **20**, 8446 (2020).

[70] A. Rossi, C. Johnson, J. Balgley, J. C. Thomas, L. Francaviglia, R. Dettori, A. K. Schmid, K. Watanabe, T. Taniguchi, M. Cothrine, D. G. Mandrus, C. Jozwiak, A. Bostwick, E. A. Henriksen, A. Weber-Bargioni, and E. Rotenberg, Direct visualization of the charge transfer in a graphene/$\alpha-$RuCl$_3$ heterostructure via angle-resolved photoemission spectroscopy, Nano Lett. **23**, 8000 (2023).

[71] S.-J. Wang, M. Panhans, I. Lashkov, H. Kleemann, F. Caglieris, D. Becker-Koch, J. Vahland, E. Guo, S. Huang, Y. Krupskaya, Y. Vaynzof, B. Büchner, F. Ortmann, and K. Leo, Highly efficient modulation doping: A path toward superior organic thermoelectric devices, Sci. Adv. **8**, eabl9264 (2022).

[72] D. Lee, J. J. Lee, Y. S. Kim, Y. H. Kim, J. C. Kim, W. Huh, J. Lee, S. Park, H. Y. Jeong, Y. D. Kim, and C.-H. Lee, Remote modulation doping in van der Waals heterostructure transistors, Nat. Electron. **4**, 664 (2021).

[73] A. K. Geim and I. V. Grigorieva, Van der Waals heterostructures, Nature (London) **499**, 419 (2013).

[74] A. Castellanos-Gomez, X. Duan, Z. Fei, H. R. Gutierrez, Y. Huang, X. Huang, J. Quereda, Q. Qian, E. Sutter, and P. Sutter, Van der Waals heterostructures, Nat. Rev. Methods Primers **2**, 58 (2022).

[75] M.-L. Lin, Y. Zhou, J.-B. Wu, X. Cong, X.-L. Liu, J. Zhang, H. Li, W. Yao, and P.-H. Tan, Cross-dimensional electron-phonon coupling in van der Waals heterostructures, Nat. Commun. **10**, 2419 (2019).

[76] Y. Li, X. Zhang, J. Wang, X. Ma, J.-A. Shi, X. Guo, Y. Zuo, R. Li, H. Hong, N. Li, K. Xu, X. Huang, H. Tian, Y. Yang, Z. Yao, P. Liao, X. Li, J. Guo, Y. Huang, P. Gao *et al.*, Engineering interlayer electron–phonon coupling in WS$_2$/BN heterostructures, Nano Lett. **22**, 2725 (2022).

[77] C. M. Chow, H. Yu, A. M. Jones, J. Yan, D. G. Mandrus, T. Taniguchi, K. Watanabe, W. Yao, and X. Xu, Unusual exciton–phonon interactions at van der Waals engineered interfaces, Nano Lett. **17**, 1194 (2017).

[78] C. Jin, J. Kim, J. Suh, Z. Shi, B. Chen, X. Fan, M. Kam, K. Watanabe, T. Taniguchi, S. Tongay, A. Zettl, J. Wu, and F. Wang, Interlayer electron–phonon coupling in WSe$_2$/hBN heterostructures, Nat. Phys. **13**, 127 (2017).

[79] L. Fu, Y. Sun, N. Wu, R. G. Mendes, L. Chen, Z. Xu, T. Zhang, M. H. Rümmeli, B. Rellinghaus, D. Pohl, L. Zhuang, and L. Fu, Direct growth of MoS$_2$/h-BN heterostructures via a sulfide-resistant alloy, ACS Nano **10**, 2063 (2016).

[80] Z. Zhang, X. Ji, J. Shi, X. Zhou, S. Zhang, Y. Hou, Y. Qi, Q. Fang, Q. Ji, Y. Zhang, M. Hong, P. Yang, X. Liu, Q. Zhang, L. Liao, C. Jin, Z. Liu, and Y. Zhang, Direct chemical vapor deposition growth and band-gap characterization of MoS$_2$/h-BN van der Waals Heterostructures on Au foils, ACS Nano **11**, 4328 (2017).

[81] A. Yan, J. Velasco, Jr., S. Kahn, K. Watanabe, T. Taniguchi, F. Wang, M. F. Crommie, and A. Zettl, Direct growth of single- and few-layer MoS$_2$ on h-BN with preferred relative rotation angles, Nano Lett. **15**, 6324 (2015).

[82] S. Nosé, A unified formulation of the constant temperature molecular dynamics methods, J. Chem. Phys. **81**, 511 (1984).

[83] A. Pulkin and O. V. Yazyev, Spin- and valley-polarized transport across line defects in monolayer MoS$_2$, Phys. Rev. B **93**, 041419(R) (2016).

[84] X. Li, S. Zhang, H. Huang, L. Hu, F. Liu, and Q. Wang, Unidirectional spin–orbit interaction induced by the line defect in monolayer transition metal dichalcogenides for high-performance devices, Nano Lett. **19**, 6005 (2019).

[85] B. Schuler, D. Y. Qiu, S. Refaely-Abramson, C. Kastl, C. T. Chen, S. Barja, R. J. Koch, D. F. Ogletree, S. Aloni, A. M. Schwartzberg, J. B. Neaton, S. G. Louie, and A. Weber-Bargioni, Large spin-orbit splitting of deep in-gap defect states of engineered sulfur vacancies in monolayer WS$_2$, Phys. Rev. Lett. **123**, 076801 (2019).

[86] Y. Wang, L. Deng, Q. Wei, Y. Wan, Z. Liu, X. Lu, Y. Li, L. Bi, L. Zhang, H. Lu, H. Chen, P. Zhou, L. Zhang, Y. Cheng, X. Zhao, Y. Ye, W. Huang, S. J. Pennycook, K. P. Loh, and B. Peng, Spin-valley locking effect in defect states of monolayer MoS$_2$, Nano Lett. **20**, 2129 (2020).

[87] E. Mitterreiter, B. Schuler, A. Micevic, D. Hernangómez-Pérez, K. Barthelmi, K. A. Cochrane, J. Kiemle, F. Sigger, J. Klein, E. Wong, E. S. Barnard, K. Watanabe, T. Taniguchi, M. Lorke, F.

Jahnke, J. J. Finley, A. M. Schwartzberg, D. Y. Qiu, S. Refaely-Abramson, A. W. Holleitner *et al.*, The role of chalcogen vacancies for atomic defect emission in MoS_2, Nat. Commun. **12**, 3822 (2021).

[88] J. Zak, Berry's phase for energy bands in solids, Phys. Rev. Lett. **62**, 2747 (1989).

[89] M. Atala, M. Aidelsburger, J. T. Barreiro, D. Abanin, T. Kitagawa, E. Demler, and I. Bloch, Direct measurement of the Zak phase in topological Bloch bands, Nat. Phys. **9**, 795 (2013).

[90] V. Mourik, K. Zuo, S. M. Frolov, S. R. Plissard, E. P. A. M. Bakkers, and L. P. Kouwenhoven, Signatures of Majorana fermions in hybrid superconductor-semiconductor nanowire devices, Science **336**, 1003 (2012).

[91] A. Das, Y. Ronen, Y. Most, Y. Oreg, M. Heiblum, and H. Shtrikman, Zero-bias peaks and splitting in an Al–InAs nanowire topological superconductor as a signature of Majorana fermions, Nat. Phys. **8**, 887 (2012).

[92] S. Kezilebieke, M. N. Huda, V. Vaňo, M. Aapro, S. C. Ganguli, O. J. Silveira, S. Głodzik, A. S. Foster, T. Ojanen, and P. Liljeroth, Topological superconductivity in a van der Waals heterostructure, Nature (London) **588**, 424 (2020).

[93] P. M. M. C. de Melo, Z. Zanolli, and M. J. Verstraete, Optical signatures of defect centers in transition metal dichalcogenide monolayers, Adv. Quantum Technol. **4**, 2000118 (2021).

[94] Q. Qian, W. Wu, L. Peng, Y. Wang, A. M. Z. Tan, L. Liang, S. M. Hus, K. Wang, T. H. Choudhury, J. M. Redwing, A. A. Puretzky, D. B. Geohegan, R. G. Hennig, X. Ma, and S. Huang, Photoluminescence induced by substitutional nitrogen in single-layer tungsten disulfide, ACS Nano **16**, 7428 (2022).

[95] M. A. U. Absor, I. Santoso, Harsojo, K. Abraha, H. Kotaka, F. Ishii, and M. Saito, Strong Rashba effect in the localized impurity states of halogen-doped monolayer $PtSe_2$, Phys. Rev. B **97**, 205138 (2018).

[96] S. Li, G. Thiering, P. Udvarhelyi, V. Ivády, and A. Gali, Carbon defect qubit in two-dimensional WS_2, Nat. Commun. **13**, 1210 (2022).

[97] C. Chen, K. Jiang, Y. Zhang, C. Liu, Y. Liu, Z. Wang, and J. Wang, Atomic line defects and zero-energy end states in monolayer Fe(Te,Se) high-temperature superconductors, Nat. Phys. **16**, 536 (2020).

[98] Y. Zhang, K. Jiang, F. Zhang, J. Wang, and Z. Wang, Atomic line defects and topological superconductivity in unconventional superconductors, Phys. Rev. X **11**, 011041 (2021).